

# Analyzing the topography of the CCR5 coreceptor using electron microscopy images of cell surface replicas with nanometer-scale electron-dense probes

Manos Protonotarios

Supervisors:

Mark Marsh, LMCB, MRC Cell Biology Unit & Department of Developmental Biology, UCL

Lewis Griffin, Computer Science Department & CoMPLEX, UCL

CoMPLEX

Essay Three,

May 11, 2011

Word Count<sup>1</sup>: 4981

---

<sup>1</sup> without figures, tables, displayed equations, references, acknowledgments and appendices

Page intentionally left blank

## Contents

1	Abstract.....	5
2	Introduction.....	5
3	Biological Background.....	6
3.1	Cell Plasma Membrane .....	6
3.1.1	Basic Structure .....	6
3.1.2	Flexibility and Fluidity of the Cell Plasma Mebrane .....	6
3.1.3	Membrane Proteins.....	6
3.2	Receptors .....	7
3.3	Endocytosis .....	8
3.4	Viruses.....	9
3.5	Human Immunodeficiency Virus (HIV).....	10
3.6	CCR5 coreceptor .....	11
4	Methods.....	13
5	Mathematical Tools and Methods .....	14
5.1	Localization of the nanoprobes.....	15
5.2	Hopkins Statistics .....	19
5.3	Ripley-based Statistics .....	20
6	Data Analysis .....	22
6.1	Nanoprobe Density.....	22
6.2	Hopkins Statistics .....	24
6.3	Ripley's K function.....	27
6.4	Ripley's H function.....	27
6.5	Clustering Analysis .....	29
7	Simulation Cases.....	30
7.1	Hopkins Statistics .....	30
7.2	Ripley's K function.....	31
7.3	Ripley's H function.....	32
7.4	Simulation Cases Analysis .....	33
8	Discussion .....	34
9	Conclusions.....	35
10	Acknowledgements.....	35

11	Appendix (Analyzed Micrographs).....	36
12	References .....	40

## 1 Abstract

We analyzed the topography of the CCR5 coreceptor on the cell surface using electron microscopy images of cell surface replicas which were acquired during previous studies at the Medical Research Council Laboratory for Molecular Cell Biology (MRC LMCB), University College London [1]. RBL and CHO cell lines transfected to express human CCR5 coreceptor (treated with RANTES or untreated) were labeled with an anti-CCR5 antibody and protein A conjugated to 15nm electron-dense gold probes. Whole mount replicas of the labeled cells were imaged by transmission electron microscopy (TEM). We used previously developed software (ImageJ) to extract the spatial coordinates of these probes and applied spatial statistics methodology in order to affirm their clustering by implementing MATLAB code.

## 2 Introduction

Human Immunodeficiency Virus (HIV) is associated with the Acquired Immunodeficiency Syndrome (AIDS). According to UNAIDS the number of adults and children to be newly infected by HIV in 2008 worldwide is 2.7 million while in the same year 2 million people died because of the infection. [2] HIV infects CD4+ helper T cells and macrophages. Depletion of the helper T cell population leads to a collapse in the immune system and the patient succumbs to opportunistic infections.

HIV entry to target cells is a multistep procedure and each of these steps offers a possible point of intervention to hinder virus entry. CCR5 is a chemokine cell surface receptor (coreceptor) involved in the HIV entry typically in the early stages of infection. The chemokine ligands trigger signaling responses and induce internalization of these receptors to down-modulate CCR5 cell surface expression. [3] The understanding of the underlying mechanisms of this receptor-induced endocytosis as well as the later fate of receptors (recycling, resensitisation etc) is crucial in the attempts to prevent viral entry.

In this study we have analyzed the topography of the CCR5 coreceptor in untreated and chemokine (RANTES) treated cells lines. This allows us to examine the steady-state behavior of CCR5 at the plasma membrane and to quantify the ligand induced clustering that occurs prior to receptor endocytosis.

## 3 Biological Background

### 3.1 Cell Plasma Membrane

#### 3.1.1 Basic Structure

The cell plasma membrane acts as a highly selective barrier preventing molecules from the extracellular environment mixing with those of the interior of the cell. Its structure is based on a *lipid bilayer* composed of two parallel apposed sheets of lipid molecules of a hydrophilic head (phospholipid) and one or two hydrophobic tails (hydrocarbon). The two parallel sheets are arranged in such a way as to minimize the energy cost in the aqueous environment of the extracellular space or the cytosol, with the hydrophilic heads facing the water at both sides of the membrane while the hydrophobic tails remaining shielded from the water in the interior of the membrane. Internal membranes of intracellular compartments forming the various organelles of eukaryotic cells have structure based on the same principles with small differences in their composition. Mass spectrometry analysis of membrane lipids has revealed that a typical cell membrane can contain more than 500 different lipid species. [4][5]

#### 3.1.2 Flexibility and Fluidity of the Cell Plasma Membrane

The cell plasma membrane has the ability to bend (*flexibility*) but also can behave as a two-dimensional fluid allowing molecules to move within the plane of the bilayer (*fluidity*). The fluidity at a given temperature depends mainly on the nature of the hydrocarbon tails (their length and the number of their double bonds) and on the phospholipid composition. Sterol cholesterol, constituting approximately 20% by weight of the membrane lipids at animal cells, modulates the membrane fluidity by filling the spaces left by neighboring phospholipids making the bilayer stiffer and less permeable. Fluidity is a crucial property of the plasma membrane as it enables the diffusion of the membrane lipids and proteins on the plane of the bilayer so after their synthesis in one site they are able to move to other regions of the cell and also facilitates the interaction between proteins (cell signaling). Additionally, fluidity is necessary for different membranes fusion and the mixing of their molecules. [4][5]

#### 3.1.3 Membrane Proteins

Most of the functional properties of a cell membrane are defined by proteins that are located on the lipid bilayer. There is a great variety in the amount and the types of proteins that usually populate the membrane (typically there are about 50 lipid molecules for each protein molecule) and this variation extends also to the structure and to the way they associate with the lipid bilayer. [4][5]

*Transmembrane* proteins, having both hydrophilic and hydrophobic regions, extend to both sides of the bilayer. The hydrophilic regions are exposed to the aqueous intracellular and extracellular environment while the hydrophobic regions remain shielded within the interior of the membrane. *Monolayer-associated* proteins are associated with the inner leaflet of the membrane (by an amphiphilic  $\alpha$  helix) and are located entirely in the cytosol. *Lipid-linked* proteins are covalently attached to a lipid group and lie outside the bilayer at the inner or at the outer side. Some other proteins are attached

with non-covalent bonds to other membrane proteins (*protein-attached*) and are thus indirectly bound to the membrane. Due to the nature of this interaction, they can be easily released from the membrane with gentle extraction procedures (*peripheral membrane proteins*) while the proteins whose attachment to the membrane relates directly to the hydrophobic region of the bilayer cannot be detached without the disruption of the bilayer (*integral membrane proteins*). The lipid-linked proteins in the case 6 of Figure 3-1 are made in the endoplasmic reticulum (ER) where the transmembrane part is cleaved off and a glycosylphosphatidylinositol (GPI) anchor is added to link the protein with the noncytosolic surface of the membrane. The protein is then transported to the plasma membrane by transport vesicles. [4][5]

Membrane invaginations (*clathrin coated pits, caveolae*) and *lipid rafts* are among the various subdomains of clustered macromolecules that can be identified on the plasma membrane. Lipid rafts are dynamic and transient structures of nanometer order, rich in cholesterol, sphingolipids and GPI-anchored proteins. [6][7]

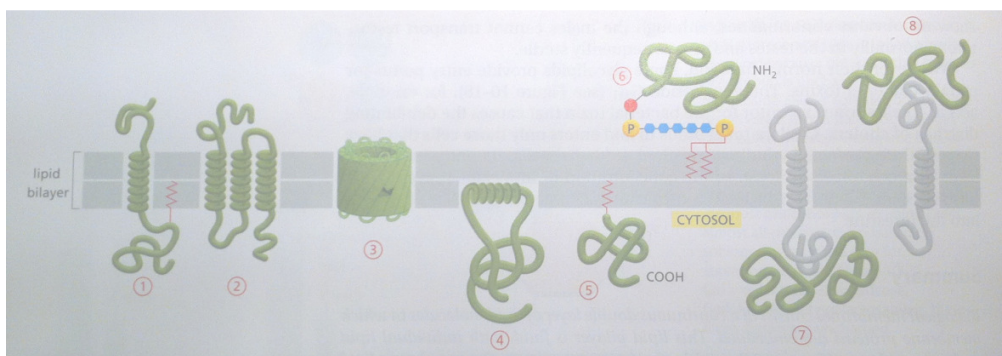


**Figure 3-1.** Association of membrane proteins with the lipid bilayer. Transmembrane proteins - 1: single  $\alpha$  helix (shown with an attached fatty acid inserted in the lipid monolayer), 2: multiple  $\alpha$  helices, 3: rolled-up  $\beta$  sheet. Proteins exposed at one side of the membrane – 4: anchored to the cytosolic monolayer by an amphiphilic  $\alpha$  helix, 5: attached to the cytosolic monolayer by a lipid chain with a covalent bond, 6: attached to the extracellular monolayer through an oligosaccharide linker, to phosphatidylinositol (GPI anchor). Other proteins are attached with non-covalent bonds to other membrane proteins (cases 7, 8) (From [5])

### 3.2 Receptors

“Any protein that binds a specific signal molecule (*ligand*) and initiates a response in the cell is called *receptor*.” [5] They can be in the cytosol or on the cell surface. Cell surface receptors have an extracellular domain where ligand binds (e.g. growth factors, adhesion molecules), a transmembrane domain and a cytosolic domain. [8] Crucial dynamic properties of the cell such as growth, contraction, secretion, adhesion, survival, differentiation and proliferation depend on the activation of receptors. Receptors transmit information from the extracellular environment by binding specific ligands and triggering intracellular signaling cascades. The analysis of their function is difficult as receptors interact with other cell surface molecules and continuously undergo events such as internalization, recycling and degradation (*trafficking*). [8][9]

According to the transduction mechanism that receptors use, they are divided into three categories: 1) Ion-channel-coupled, controlling the flow of ions, 2) G-protein-coupled, activating membrane-bound GTP-binding proteins which in turn activate an ion channel or an enzyme triggering other effects and 3) Enzyme-coupled, acting as enzymes or associating with enzymes inside the cell. [4]

### 3.3 Endocytosis

Through *endocytosis*, cells import materials from the extracellular medium. Macromolecules, specific substances, other cells or even viruses get enclosed in small invaginations of the cell membrane which eventually pinch off forming endocytic vesicles. According to the size of the vesicles, endocytosis can be characterized as *phagocytosis* when large particles, generally larger than 250nm in diameter are ingested or as *pinocytosis* when smaller vesicles of about 100nm in diameter ingest fluid and solutes. Almost every eukaryotic cell participates in this process of endocytosis, ingesting parts of its own membrane. Since, on average, its surface area remains constant, a converse process of *exocytosis* takes place at the same time delivering endocytic vesicle membrane pieces back to the original cell membrane by fusion, in a state of dynamic equilibrium. [4][5]

Ligand uptake by *receptor-mediated endocytosis* provides a more efficient way for selective internalization of material. Since specific macromolecules trigger the endocytosis by binding to the appropriate surface receptors, they can be internalized in more than 1000-fold greater concentration compared to ordinary endocytosis, minimizing, at the same time, the amount of the taken up extracellular fluid. [4][5] Apart from taking up nutrients, cells use this mechanism to respond to external stimuli and modulate the expression of cell membrane molecules. The most commonly used and well characterized mode of receptor uptake is *clathrin-mediated endocytosis*. Polygonal coats of clathrin triskellion (heterotrimeric clathrin complexes that form the clathrin lattices) are formed on the cytosolic side of the plasma membrane. These initiate as pits that invaginate and finally pinch off as free clathrin-coated vesicles (CCVs). [10][11]

Cell surface receptors are selected for clathrin-mediated endocytosis via specific protein motifs, following internalization they are targeted to different pathways depending on their type. Receptors that are not retrieved from the early endosomes are degraded at the lysosomes. Those that are retrieved can return to their original plasma membrane domain (*recycling*) or be directed to a different one (*transcytosis*). The ligand is normally dissociated in the endosome or degraded in the lysosomes unless it stays attached to the receptor in which case both follow a common pathway. [4][10][11]

Among non-clathrin dependent types of endocytosis are micropinocytosis and caveolar. Figure 3-2 depicts the possible endocytosis pathways.

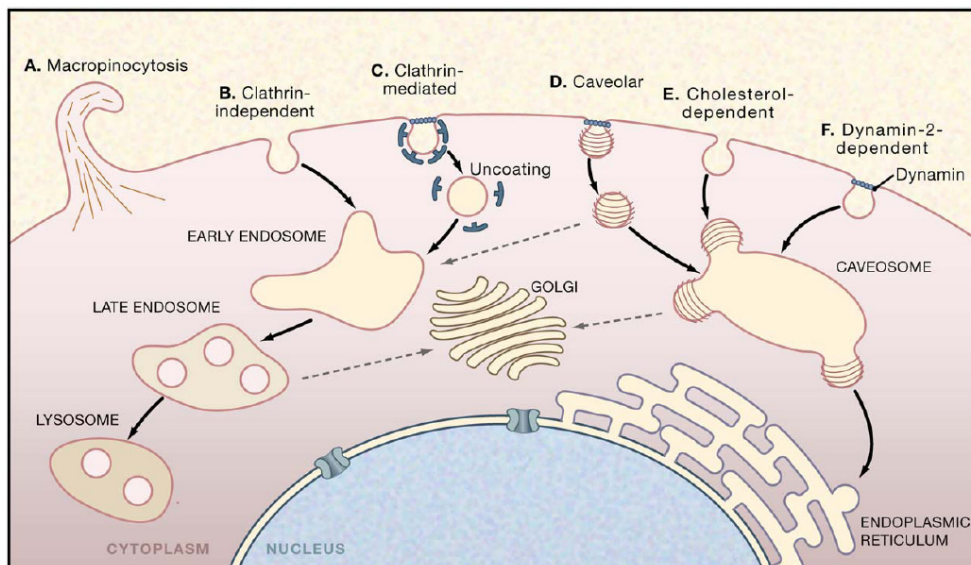


**Figure 3-2.** Six pathways of endocytosis. (A): Macropinocytosis (B): Clathrin-independent pathway (C): Clathrin-mediated pathway, (D): Caveolar pathway (cholesterol-dependent), (E): Cholesterol-dependent endocytic pathway without clathrin or caveolin-1, (F): Pathway similar to (D) but dependent on dynamin-2 (From [12])

### 3.4 Viruses

Viruses are very small and have relatively simple structures. Their metabolic activity depends exclusively on the host cell whose metabolites and organelles are exploited to express and replicate their genome and to generate new viruses. The *virion*, the inert virus particle of the extracellular phase of the infection cycle, contains the genome in the form of either DNA or RNA enclosed in a protein shell (*capsid*, usually helical or icosahedral) which in some cases has a lipid-rich outer coat (*envelope*). [13][14]

Viruses exploit specific receptors to interact with target cells and activate cellular responses and mechanisms such as endocytosis, trafficking and sorting. This allows virus particles to pass through membranes and other barriers and transfer their genes to the cytosol or the nucleus. [12] Initially, virions bind to *attachment factors* via non-specific interactions that aggregate particles on the cell surface. *Virus receptors*, on the other hand, interact with the virion in a highly specific way with the virus particles and may initiate conformational changes of the virus particle, activate signaling pathways and evoke the endocytic internalization. The high specificity of this kind of interaction implies that only certain types of cells, presenting the required receptors, can be infected by specific viruses (*species tropism and cell tropism*). The low *affinity* of the latter interactions is often overcome with the existence of multiple binding sites which give rise to higher *avidity* and may also lead to the clustering of the receptors. [12]

### 3.5 Human Immunodeficiency Virus (HIV)

Human Immunodeficiency Virus (types HIV-1 and HIV-2) is associated with the Acquired Immunodeficiency Syndrome (AIDS). HIV infects CD4+ helper T cells, macrophages and dendritic cells. [2][13]

HIV is a *retrovirus* and as such has enveloped particles. Retroviruses contain two identical strands of an RNA genome which with an RNA-dependant DNA polymerase (*reverse transcriptase*) is transcribed to DNA which becomes incorporated in the host's cell genome via the protein *integrase* function. [13][14]

The viral envelope contains glycoprotein trimers consisting of 3 pairs of gp41 and gp120 subunits associated via non-covalent interactions within gp41. The heavily glycosylated gp120 subunit is external and contains the receptor binding sites. The gp41 contains a hydrophobic peptide that is involved in the membrane fusion. [3][15]

HIV enters target cells by a multistep procedure. Firstly, the gp120 subunit of the envelope binds to the CD4 receptor initiating conformational changes of the envelope protein which reveal a hidden highly conserved domain that is able to bind to another receptor (coreceptor). During the initial stage of the infection the dominant coreceptor used by the virus is CCR5 while mutations in the viral envelope at later stages make possible the use of the CXCR4 coreceptors in addition to CCR5. [3][15][16] After the binding of the gp120 subunit, conformational changes of gp41 lead to the insertion of the fusion peptide in the cell membrane, the binding of the gp41 to the coreceptor and the deformation of the viral and target cell membranes which are brought together by mechanical forces exerted by the helical regions of the gp41 (Figure 3-3). [3] This is thought to promote fusion at the plasma membrane allowing access to the cytosol. Although endocytic uptake of HIV particles takes place, it was considered nonproductive because of virus degradation in the lysosomes. Recent studies, however, show that endocytosis is a possible alternative way for HIV productive entry. [17][18][19]

HIV-1 variants are characterized as X4 if they are CXCR4 specific; R5 if they are CCR5 specific and R5X4 if they can use both the CCR5 and CXCR4 coreceptors (Figure 3-4). However, not all features of HIV tropism can be explained by this differentiation since some additional chemokine receptors are involved in HIV-1 activity. [15]

Only 10% of the CD4+ cells present CCR5 coreceptors while 90% of the CD4+ present CXCR4 coreceptors. Therefore, mutations in the viral envelope that allow binding to CXCR4 coreceptor lead to accelerated disease progression. [3]

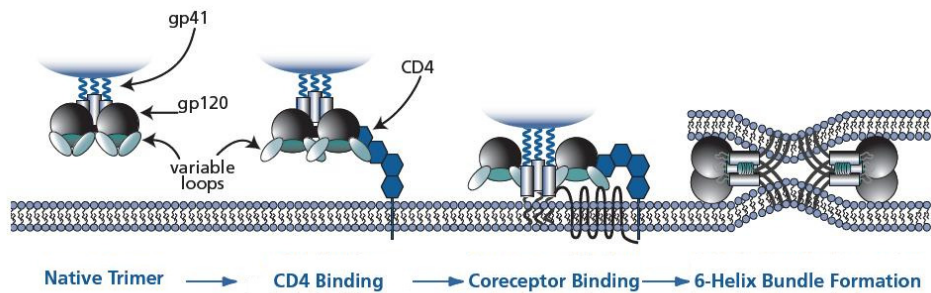


Figure 3-3. Steps of HIV entry into target cells. (From [3])

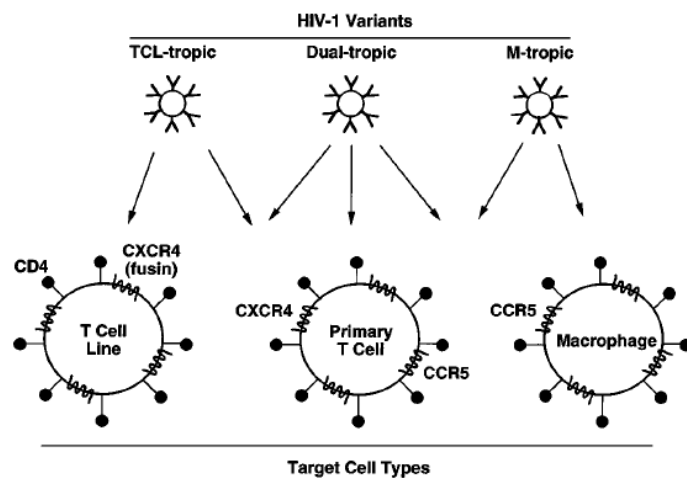


Figure 3-4. HIV-1 tropism. TCL-tropic strains (X4) are specific for CXCR4. M-tropic strains (R5) are specific for CCR5 and dual tropic strains (R5X4) can bind to both CXCR4 and CCR5. The types of cells that can be infected are shown with the arrows (left to right: CD4+ T cell lines, primary CD4+ T cells and macrophages). (From [15])

### 3.6 CCR5 coreceptor

The family of G-protein coupled receptors (GPCRs) is the largest family of cell surface receptors. They respond to a great variety of signal molecules (proteins, small peptides, derivatives of amino acids or fatty acids) with a different receptor for each. They all have a similar structure of a single polypeptide chain crossing the cell membrane seven times (Figure 3-5). The portion in the cytosol binds to the G protein complex, which mediates signal transduction, while the extracellular domain with some part of the transmembrane portion binds the ligand. [4]

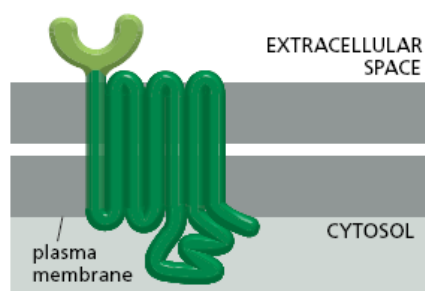


Figure 3-5. G-protein-coupled receptor. (From [4])

*Chemokine receptors* is a category of GPCRs which signal when they bind one or more members of the chemokine superfamily of *chemotactic cytokines* (small peptides). Each chemokine receptor has different chemokine specificity. The fact that some receptors can bind multiple chemokines and that some chemokines can bind multiple receptor subtypes leads to significant overlapping of their specificities. [20]

CXCR4 is the only chemokine receptor proven essential for life and it was the first one discovered as an HIV-1 coreceptor. It is widely expressed on hematopoietic cell types (T cells, macrophages, T lymphocytes, blood derived dendritic cells etc). [20] CCR5 being a major HIV-1 coreceptor is expressed on T lymphocytes and macrophages. MIP-1 $\alpha$ , RANTES (regulated on activation normal T cell expressed and secreted), MIP-1 $\beta$  and MCP-2 are high affinity ligands and high-potency agonists of CCR5. [20]

Agonist occupancy of GPCRs leads to the removal of the surface receptors via endocytosis and results in down-modulation of its responsiveness. Intrinsic properties of the receptor determine the efficiency of this down-modulation which is the combined result of receptor internalization, sequestration, recycling and degradation. [21]

Importantly, ligand induced down modulation of CXCR4 and CCR5 is able to protect cells from HIV infection. For instance, phorbol esters increase the endocytosis of CXCR4 leading to a 60-90% reduction in cell surface expression. [22] CXCR4 was localized in endosomal compartments after internalization through coated pits and coated vesicles while removal of the phorbol ester resulted in the recycling of the receptor to the cell surface. [23]

Primary cells expressing endogenous CCR5 (peripheral blood mononuclear cells, purified human CD4<sup>+</sup> T cells) and cells such as CHO (Chinese Hamster Ovary) and RBL (Rat Basophilic Leukaemia) transfected to express CCR5 coreceptor exhibited rapid endocytosis and internalization of the CCR5 coreceptors after agonist stimulation (RANTES and AOP<sup>1</sup> RANTES). Internalization occurred in a clathrin dependent manner and was preceded by receptor clustering within flat clathrin

---

<sup>1</sup> AOP: aminoxy pentane

lattices. Removal of RANTES allowed internalized CCR5 to recycle and become sensitive to further cycles of induced endocytosis while the same did not happen with AOP RANTES where most CCR5 remained internalized. [21][23]

We have studied the distribution of CCR5 in untreated cells and those treated with ligand (RANTES) to induce receptor clustering and internalization. By examining the behaviour of CCR5 at the plasma membrane we may better understand the cell biology of the receptor and how HIV exploits it to enter target cells.

## 4 Methods

The different cell lines analyzed are shown in Table 4-1: Rat Basophilic Leukaemia (RBL) cells expressing CCR5 and Chinese Hamster Ovary (CHO) cells expressing human CCR5.

Cell Type	Expt#	Micrographs	Scanned Images
RBL CCR5 Untreated	WM537	5702, 5703, 5704, 5705, 5708	DATA-07042011-A001
RBL CCR5 RANTES	WM539	5727, 5694, 5692, 5691, 5690	DATA-07042011-B001
CHO CCR5 Untreated	WM481	5042, 5043, 5046, 5048, 5049	DATA-07042011-C001
CHO CCR5 RANTES	WM476	5026, 5027, 5033, 5031, 5036	DATA-07042011-D001

**Table 4-1.** Different cell lines used for the analysis with the name of the micrographs and the scanned images. [1]

The procedure followed in previous study [1] is described here briefly: Cells were grown on glass coverslips, were rinsed in Buffer Saline (BM) and incubated at 37°C in BM or in BM containing 125 nM RANTES (CCL5) for 2 minutes. After fixing with Paraformaldehyde (PFA)/Guteraldehyde (GA), CCR5 at the cell surface was labeled with MC-5 antibody (7.7nM) and cells were incubated with Protein A which was conjugated to gold particles of 15nm diameter (PAG<sub>15</sub>). After fixing in GA cells dehydrated and critical point dried. A film of platinum/carbon was sputtered at an angle of 45° to create contrast of the membrane morphology and a thicker layer of carbon was sputtered to reinforce the replicas. After scoring them in small squares to fit the Electron Microscopy (EM) grid, Hydrofluoric acid was used to detach them from the glass and Sodium Hydroxide to digest the remaining cellular material. The replicas were then scanned under the Electron Microscope (TEM) and micrographs were taken as shown in Table 4-1. [1] For the whole series of image files see Appendix.

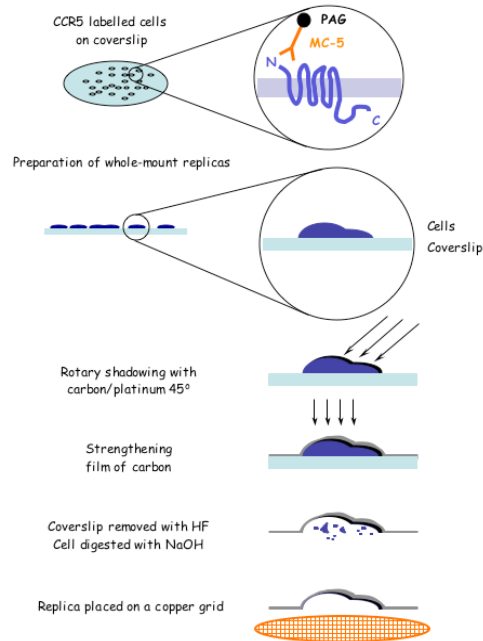


**Figure 4-1.** Whole mount preparation of cell surface replicas. (From [1])

## 5 Mathematical Tools and Methods

The mathematical tools used for the quantification of the distribution of the nanoprobe are spatial statistics and cluster analysis. The main course of the present analysis is similar to that conducted in [9]. Two main statistics are employed: The Hopkins statistics and the Ripley based statistics. The studied cases are tested against the null Hypothesis  $H_0$  of Complete Spatial Randomness (CSR). A clustering algorithm is subsequently used to automatically localize clusters.

The starting point is the micrographs of cell surface replicas taken by TEM microscopy. Signaling molecules are labeled by the electron dense gold nanoparticles. In order to acquire useful information and characterize successively the regions of the cell surface, it is important to capture a relatively large area. It is also essential to include large number of nanoprobe in order to derive reliable statistics.

The application of mathematical methods using computer algorithms requires the digitization of the information at a first level by digitizing the micrographs. So, scanning of 5 micrographs for the 4 groups of different cell types and conditions was conducted at 1,600 dpi giving 16 bit (grayscale) tif type image files. The acquired images were approximately 6,000X4,500 pixels and corresponded to a magnification of 12,000.

## 5.1 Localization of the nanoprobes

The second level of digitization is the localization of the nanoprobes on the images and the exporting of their coordinates. The analyzed images were taken from the initial images by cropping a square area of side length 2,000pixels at 8bit (grayscale) without cell membrane ruptures, folds and borders. Standardizing the images simplified the subsequent analysis and the implementation of the algorithms and resulted in the same captured area of  $2.5\mu\text{m}\times 2.5\mu\text{m}$  ( $1\text{px}\leftrightarrow 1.25\text{nm}$ ) for each case.

The localization of the probes was done automatically with the use of the ImageJ plugin ParticlePicker which combines a thresholding algorithm with an estimation of the expected particle area in pixels to avoid large areas of background of the same grayscale value.

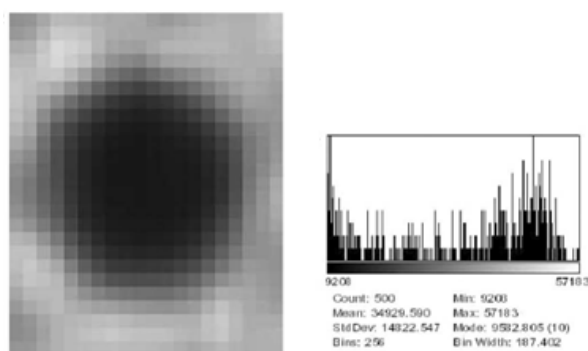


**Figure 5-1.** Typical image of a nanoprobe in a digitized image. Brightness distribution of the shown digitized image (left) is presented on the right side showing not only that the probe does not have constant grayscale value but also that the background information is inserted in the histogram.

(From [9])

Some other approaches have been employed in [9] with matched filtering algorithm (two-dimensional cross-correlation function of the original image with an image of a typical probe) giving good results for small probe sizes and top-hat transformation giving, in general, more satisfying results as it is able to handle the background brightness level in a more efficient way.

After the automatic localization of the probes a plugin for manual correction for false negative or positive localization was used with most common misidentification that of closely spaced pairs or of particles in regions with high background noise. An additional difficulty is, in general, however, the inherent distribution in nanoparticles size and shape from the manufacturer.

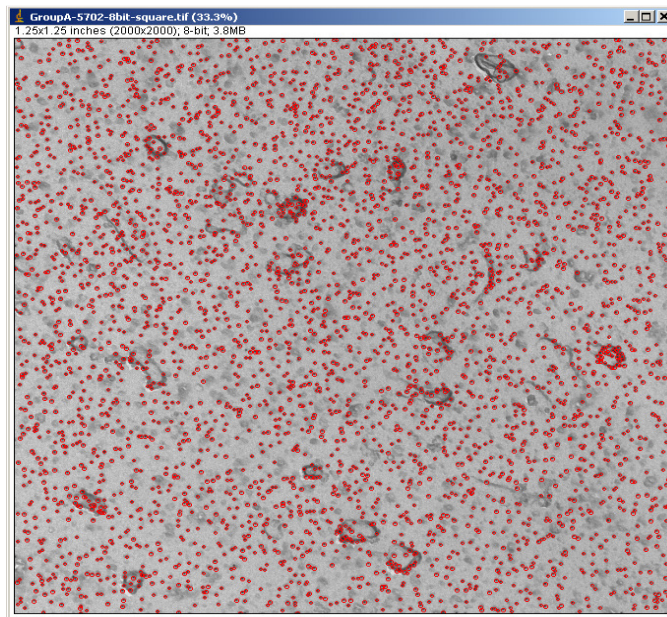


**Figure 5-2.** Superposition of the real TEM image with the localized nanoparticles after the manual correction of misidentifications. Three dimensional formations of the cell membrane (small protrusions and villi) are visible as projections on the same plane resulting in an overestimation of the probe density. (Image)

In the final images, three dimensional formations of the cell membrane (small protrusions and villi) were visible as projections on the same plane. These areas should be excluded from the analysis, since they result in an overestimation of the probe density and interfere with their true spatial statistics properties. However, further fragmenting of the images could render our statistics analysis less reliable because of edge effects and small number of probes while simply deleting of the areas would not allow the proper application of the mathematical tools (Hopkins statistics and Ripley's functions). Therefore, it was decided to keep the initial images but to erase manually the problematic regions and subsequently add by uniformly random simulation the required number of probes dictated by the calculated density from the rest of the area.

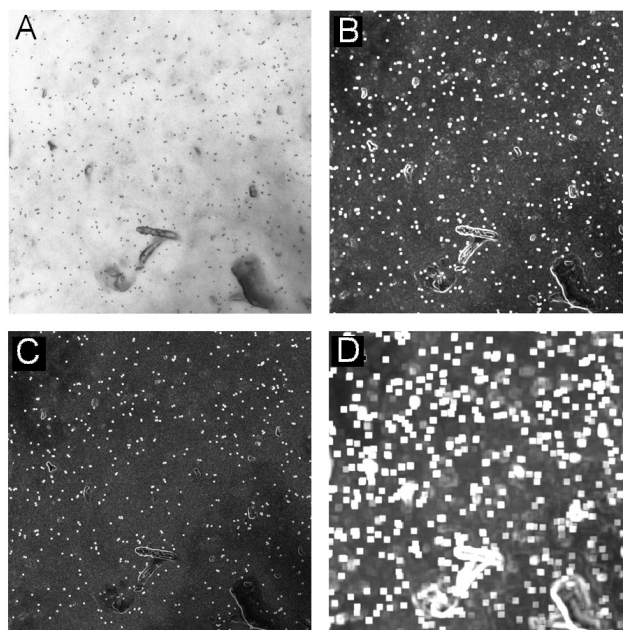


**Figure 5-3.** Attempt to automatically exclude problematic areas of the cell surface. (A): TEM image, (B),(C),(D): application of  $\sqrt{\text{blur}(\text{image}^2) - \text{blur}^2(\text{image})}$ . (B): blurring is done with simple averaging of 10 pixels, (C): blurring is done with Gaussian kernel of 4 pixels, (D): blurring is done with Gaussian kernel of 10 pixels. (Matlab)

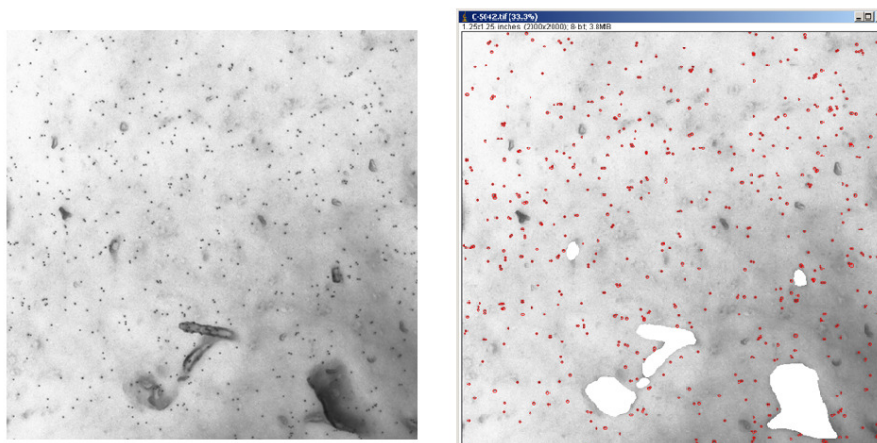


**Figure 5-4.** Real TEM image (left) and processed TEM image (right) with localized probes after manually excluding problematic areas. (ImageJ)

The images used with their dimensions, the number of localized particles, the erased area (white area), the calculated density and the number of added points in the erased areas by simulation are shown in Table 5-1.

	Image Name	X (px)	Y (px)	Area (px)	Localized Nanoparticles	White Area (%)	Density (#/px)	Density (#/um <sup>2</sup> )	Extra Random Points	Extra Random Points (%)	Total points
RBL CCR5 Untreated	A-5702	2000	2000	4000000	3556	4.05	9.26E-04	593	149	4.19	3705
	A-5703	2000	2000	4000000	2279	4.91	5.99E-04	383	117	5.13	2396
	A-5704	2000	2000	4000000	4031	5.51	1.07E-03	683	235	5.83	4266
	A-5705	2000	2000	4000000	2078	2.72	5.34E-04	342	58	2.79	2136
	A-5708	2000	2000	4000000	2222	13.73	6.44E-04	412	353	15.89	2575
RBL CCR5 RANTES	B-5690	2000	2000	4000000	1684	0.12	4.21E-04	270	1	0.06	1685
	B-5691	2000	2000	4000000	1939	0.00	4.85E-04	310	0	0.00	1939
	B-5692	2000	2000	4000000	1084	0.22	2.72E-04	174	2	0.18	1086
	B-5694	2000	2000	4000000	1444	0.00	3.61E-04	231	0	0.00	1444
	B-5727	2000	2000	4000000	1350	0.16	3.38E-04	216	2	0.15	1352
CHO CCR5 Untreated	C-5042	2000	2000	4000000	578	3.75	1.50E-04	96	22	3.81	600
	C-5043	2000	2000	4000000	667	3.11	1.72E-04	110	21	3.15	688
	C-5046	2000	2000	4000000	600	3.22	1.55E-04	99	19	3.17	619
	C-5048	2000	2000	4000000	607	1.00	1.53E-04	98	6	0.99	613
	C-5049	2000	2000	4000000	575	4.51	1.51E-04	96	27	4.70	602
CHO CCR5 RANTES	D-5026	2000	2000	4000000	447	3.69	1.16E-04	74	17	3.80	464
	D-5027	2000	2000	4000000	508	1.32	1.29E-04	82	6	1.18	514
	D-5031	2000	2000	4000000	374	0.18	9.37E-05	60	0	0.00	374
	D-5033	2000	2000	4000000	400	7.16	1.08E-04	69	30	7.50	430
	D-5036	2000	2000	4000000	298	0.08	7.46E-05	48	0	0.00	298

**Table 5-1.** Data for the five images of each of the four analyzed cases. The number of localized particles (total: 26,721, after the manual correction), the excluded (white) area, the resulting probe density and the extra added particle points from the uniformly random simulation are shown.

## 5.2 Hopkins Statistics

The Hopkins statistics is based on the comparison of nearest-neighbor distances from randomly picked probes and uniformly randomly picked points. [9] We denote  $d(p_1, p_2)$  the distance between two points  $p_1(x_1, y_1)$  and  $p_2(x_2, y_2)$ ,  $S$  the set of  $n$  total probes,  $s_j=(x_j, y_j)$  a random sampling point and  $\tilde{p}_k = p_{i_k}$  a random chosen probe.

We also define  $d(p_j, S) = \min\{d(p_j, p_k), \forall p_k \in S\}$  as the minimum distance of the point  $p_j$  from all points belonging to set  $S$ . By choosing in random  $m$  sampling points and probes we define the *Hopkins statistics* as:

$$H = \frac{U}{U + W} \quad (5-1)$$

Where  $W = \sum_{j=1}^m d^2(\tilde{p}_k, S)$  and  $U = \sum_{j=1}^m d^2(s_j, S)$ . The values of  $H$  are restricted in  $[0,1]$  with the complete random case giving  $H=0.5$  (Figure 5-5) while existence of clustering would result in higher values. [9]

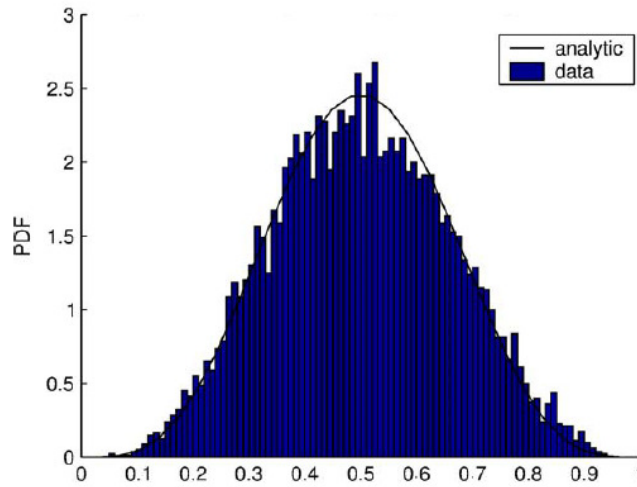


**Figure 5-5.** Histogram of Hopkins statistics of CSR simulation applying bootstrap method with number of random points and random probes  $m=5$ , repeated 1000 times shown with the theoretical curve of the

probability density function  $f(H) = \frac{H^{m-1}(1-H)^{m-1}}{\Gamma(m)^2 / \Gamma(2m)}$ , where  $\Gamma(n)=(n-1)!$  (From [9])

### 5.3 Ripley-based Statistics

We define the *intensity*  $\lambda$  as  $\lambda = \frac{n}{A(C)}$ , where  $A(C)$  is the area of a planar set  $C$ . With  $r > 0$  as a parameter we define the set  $S_p(r)$  as  $S_p(r) = \{q \in S; 0 < d(p, q) \leq r\}$  and the *indicator* for the same  $r$  as  $I_p(r) = |S_p(r)|$  (i.e. the number of probes of  $S$  that are located in a distance less than  $r$  from point  $p$ ).

The *Ripley's K function* is defined as:

$$K(r) = \frac{Av(r)}{\lambda} \quad (5-2)$$

Where  $Av(r)$  is the average indicator function for the parameter  $r$  and its expected value for the CSR

case is  $\lambda\pi r^2$ :  $Av(r) = \frac{1}{n} \sum_{i=1}^n I_{p_i}(r) \approx \lambda\pi r^2$ .

Two other forms of Ripley's  $K$  function are derived from  $K$  as:

$$L(r) = \sqrt{\frac{K(r)}{\pi}}, \text{ with expected value } r \quad (5-3)$$

and

$$H(r) \text{ or } \tilde{L}(r) = L(r) - r, \text{ with expected value } 0 \quad (5-4)$$

Divergence above the theoretical curve or the CSR simulated curve represents clustering and the value of  $r$  at maximum divergence gives an estimation of the cluster size. [9][24][25]

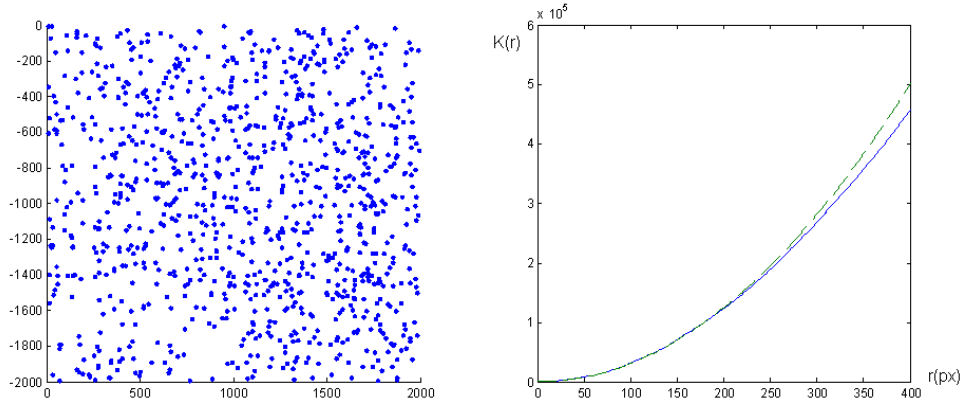


**Figure 5-6.** Simulation of the CSR case with the corresponding particle arrangement on the plane (left) and calculation of Ripley's K function (right). Significant agreement of simulated (solid blue line) and theoretical case (black dashed line) is observed. In greater detail we expect slight divergence in short distances where the probe size does not allow particle overlapping and in greater distances (observed for  $r > 250$  pixels) where the borders of the analyzed region become important. (Matlab)

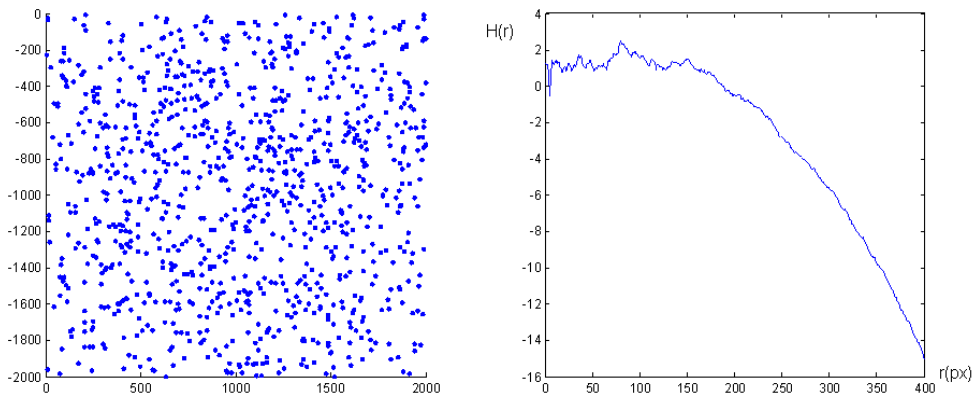


**Figure 5-7.** Simulation of the CSR case with the corresponding particle arrangement on the plane (left) and calculation of Ripley's H function (right). The simulated graph remains relatively close to zero for short distances and then presents a linear drift  $\sim -1$  due to the difference between global and local density. [9][24] (Matlab)

## 6 Data Analysis

### 6.1 Nanoprobe Density

The calculated nanoprobe density is presented in Table 6-1 and graphically in Figure 6-1.

	Image Name	Density (#/um <sup>2</sup> )	Group Density (#/um <sup>2</sup> )	s= $\sigma(N-1)$	SE
RBL CCR5 Untreated	A-5702	593	482.58	147.50	73.75
	A-5703	383			
	A-5704	683			
	A-5705	342			
	A-5708	412			
RBL CCR5 RANTES	B-5690	270	240.24	52.00	26.00
	B-5691	310			
	B-5692	174			
	B-5694	231			
	B-5727	216			
CHO CCR5 Untreated	C-5042	96	99.97	5.85	2.92
	C-5043	110			
	C-5046	99			
	C-5048	98			
	C-5049	96			
CHO CCR5 RANTES	D-5026	74	66.65	13.11	6.55
	D-5027	82			
	D-5031	60			
	D-5033	69			
	D-5036	48			

**Table 6-1.** Nanoprobe Density calculated from the five TEM images of each of the four analyzed cases and Average Group Density.

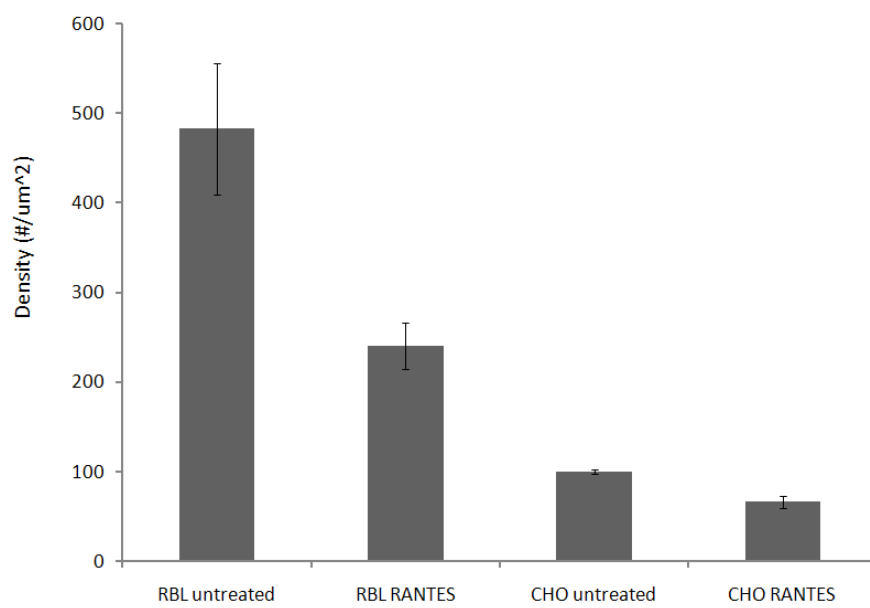


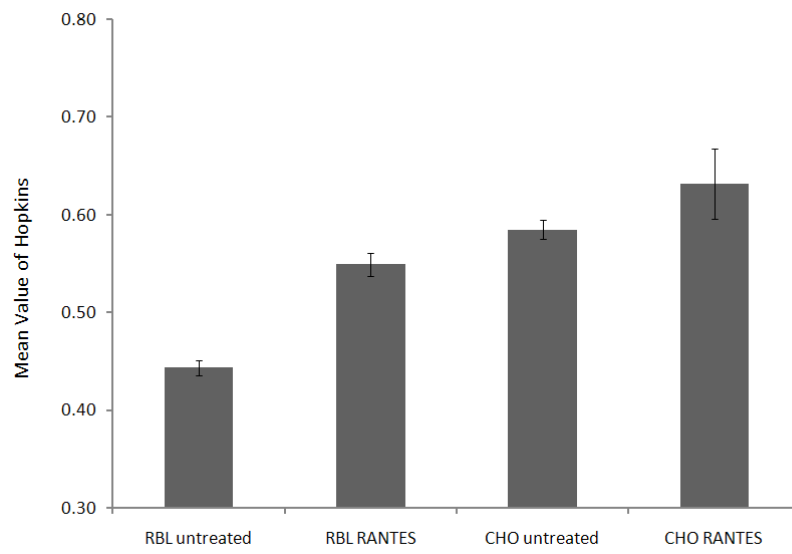
**Figure 6-1.** Average nanoprobe density (with Standard Error) calculated from the five images of each of the four analyzed cases.

## 6.2 Hopkins Statistics

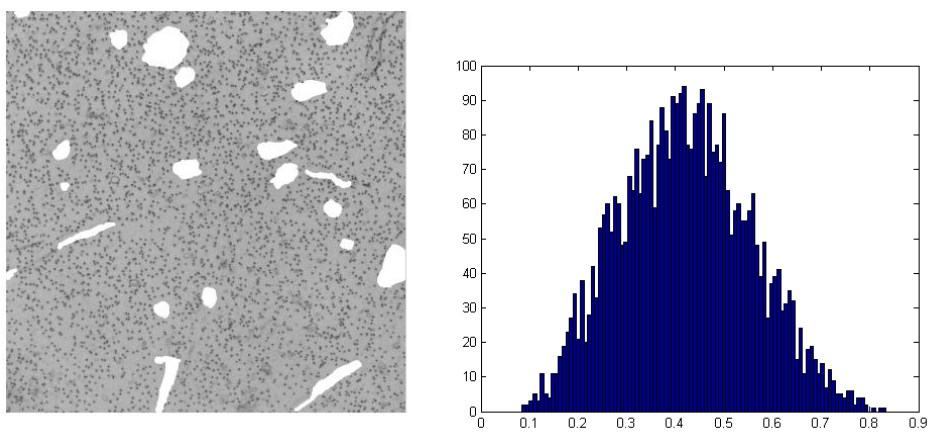
The results of the Hopkins statistics on the analyzed cases are summarized in Table 6-2 and graphically in Figure 6-2. Bootstrap method with  $m=10$  (2000 repetitions) was employed and the mean value of the Hopkins distribution was used. Thus, the null hypothesis ( $H_0$ ) of CSR was rejected with confidence  $\geq 95\%$  for all cases. The use of the position of the maximum of the (smoothed) distribution was also checked but because of the greater deviation,  $H_0$  could not be rejected in all cases. Application of the same methodology on the simulated CSR case gave  $\text{mean}(H)=0.500\pm 0.003$ . [26]

	Image Name	Hopkins Mean Value	Group Mean Value	Group Mean Value SE	Hopkins Max Position	Group Max Position	Group Max Position SE	Reject Complete Randomness (t-test)
RBL CCR5 Untreated	A-5702	0.44	0.44	0.008	0.49	0.45	0.019	99.0%
	A-5703	0.46			0.42			
	A-5704	0.42			0.48			
	A-5705	0.44			0.40			
	A-5708	0.45			0.45			
RBL CCR5 RANTES	B-5690	0.55	0.55	0.012	0.54	0.56	0.009	99.0%
	B-5691	0.52			0.56			
	B-5692	0.57			0.55			
	B-5694	0.58			0.59			
	B-5727	0.53			0.56			
CHO CCR5 Untreated	C-5042	0.60	0.58	0.009	0.57	0.59	0.020	99.9%
	C-5043	0.60			0.61			
	C-5046	0.56			0.56			
	C-5048	0.58			0.65			
	C-5049	0.58			0.56			
CHO CCR5 RANTES	D-5026	0.54	0.63	0.036	0.51	0.68	0.089	95.0%
	D-5027	0.59			0.63			
	D-5031	0.64			0.61			
	D-5033	0.65			0.68			
	D-5036	0.73			0.98			

Table 6-2. Application of Hopkins statistics and t-test for the CSR  $H_0$  rejection.



**Figure 6-2.** Mean value of Hopkins statistics (with Standard Error) indicating sparseness of particles (repulsion) for RBL untreated cells ( $H < 0.5$ ) and clustering for the rest of the cases ( $H > 0.5$ ).



**Figure 6-3.** TEM image (with deleted regions on white) (left) and the corresponding Hopkins distribution (right) revealing divergence from the CSR case. There is a slight positive skew resulting in mean value of  $H$  less than 0.5. This is indicative of dispersion of the particles resembling repulsion (RBL untreated). (Matlab)

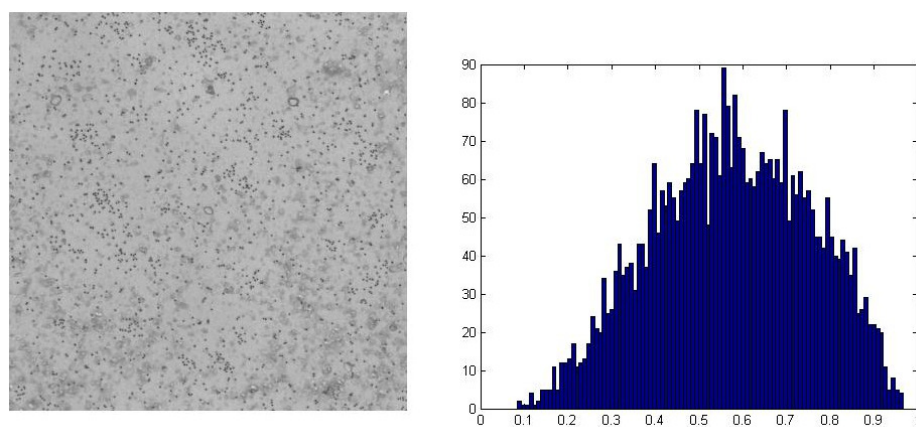


**Figure 6-4.** TEM image (without deleted region – no problematic areas) (left) and the corresponding Hopkins distribution (right) revealing divergence from the CSR case towards clustering (RBL RANTES). (Matlab)

### 6.3 Ripley's K function

The divergence of Ripley's K function from the theoretical curve validates qualitatively the results derived from Hopkins statistics. More specifically, in the case of untreated RBL cell group the experimental curve is below the theoretical curve confirming the sparseness of the spatial distribution of the probes. In the case of RANTES treated RBL cells the experimental curve is above the theoretical curve suggesting clustering. Clustering is observed similarly for both the cases of untreated and treated CHO cell groups.

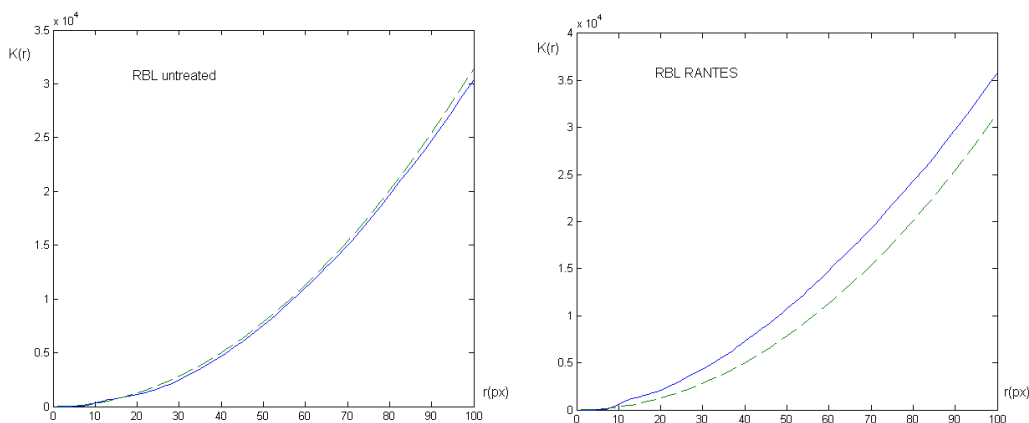


**Figure 6-5.** Ripley's K function. Slight divergence below the theoretical curve (dashed black line) indicates sparseness in the case of untreated RBL (left). Divergence above the theoretical curve (dashed black line) indicates clustering in the case of RBL RANTES (right). (Matlab)

### 6.4 Ripley's H function

Ripley's H function provides more quantifiable results than K function. As expected, there is agreement with K function. In the case of the untreated RBL cells, great similarity in the appearance of the curves is observed for all the members of the group. At  $r \sim 40$  pixels (50nm) the low values of  $H(r)$  indicate sparse placing of the particles. For RBL RANTES cells, clustering is suggested since the experimental curves reach values greater than zero (maximum values: 5-15) (Figure 6-6). For the untreated CHO cells group, clustering is validated with maximum values significantly greater than zero (maximum values: 13-18). RANTES treated CHO cells present even more clustering with greater maximum values (maximum values: 15-65) but with greater deviation as well. The shapes of the curves, in the case of untreated CHO cells, indicate clustering at a common scale while that of the treated CHO cells suggest a variety in scale clustering (Figure 6-7).

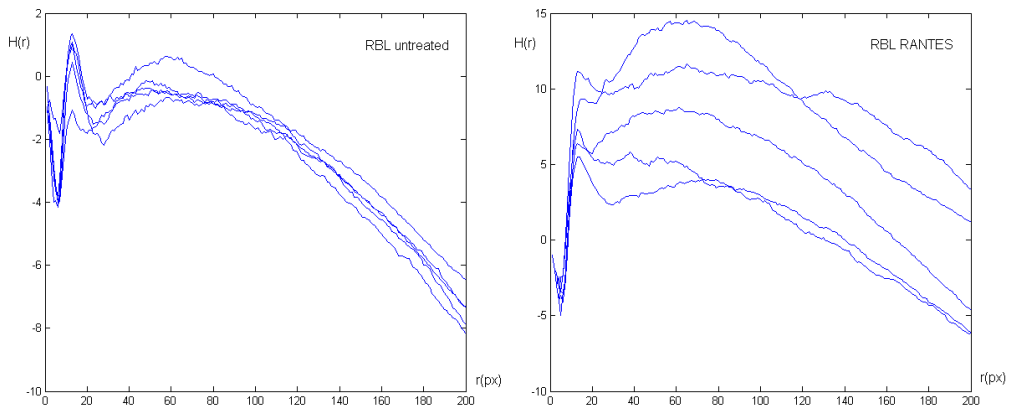


**Figure 6-6.** Ripley's H function. Values of Ripley's H function below zero indicate sparseness in the case of untreated RBL (left). At the scale of 40 pixels (~50nm) sparseness is detected. Values of Ripley's H function above zero indicate clustering in the case RBL RANTES (right). (Matlab)

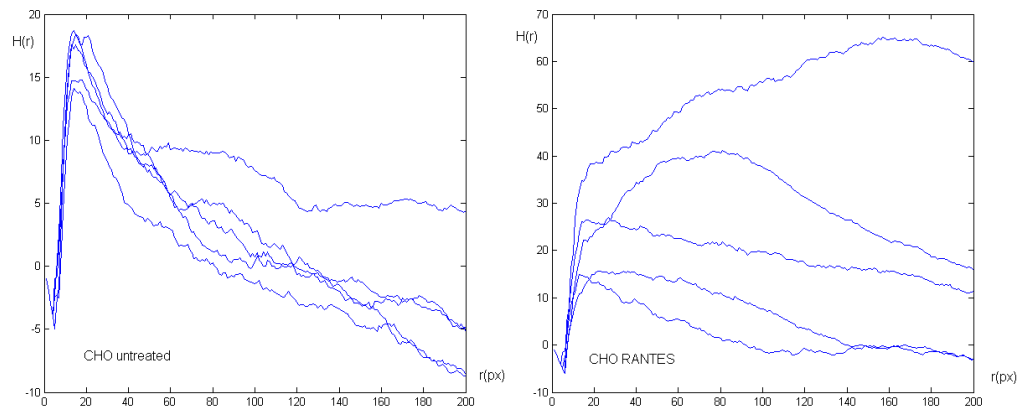


**Figure 6-7.** Ripley's H function. Values of Ripley's H function above zero indicate clustering in both untreated (left) and RANTES treated (right) CHO cells. (Matlab)

## 6.5 Clustering Analysis

Clustering analysis should be applied only after clustering has been confirmed. Here the clustering algorithm is based on the distances between the probes (inter-probe distances) and classifies two probes in the same cluster if their distance is less than the predefined cutoff distance. By trial and error and visual inspection the cutoff distance was set at 50 pixels (75nm) for the application of the clustering algorithm shown in Figure 6-8. Clustering analysis is very sensitive to this cutoff distance and a more reliable method should be implemented as it is discussed in Simulation Cases. [9]

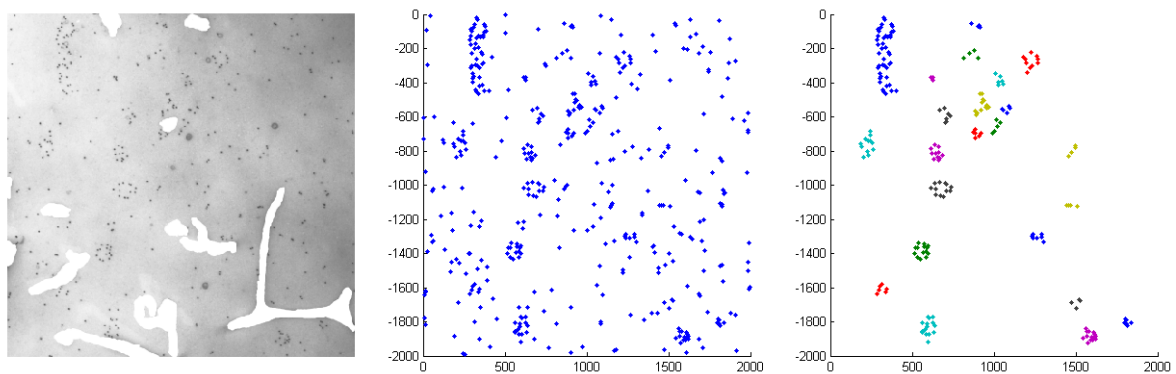


**Figure 6-8.** Clustering Analysis. TEM image of CHO cell membrane treated with RANTES (left). Arrangement on the plane of the localized and the randomly added probes in white areas which correspond to small protrusions and villi (center). Depiction of the clustering separation by the clustering algorithm using cut off distance of 50 pixels (~62nm) (right). The probes are separated in clusters shown in different colors. If clusters contain less than 4 members it is chosen not to be shown. (Matlab)

## 7 Simulation Cases

Various simulation cases were tested for both Hopkins and Ripley statistics in order to approach their limitations or test the possibility of acquiring additional information from the shape of the graphs, such as domain size. Most importantly though, simulations were used in order to validate the reliability of both statistics as a criterion for the existence of clustering (or sparseness) by examining and comparing clustered and CSR simulations. Some of the interesting simulation cases are presented briefly in the following figures.

### 7.1 Hopkins Statistics

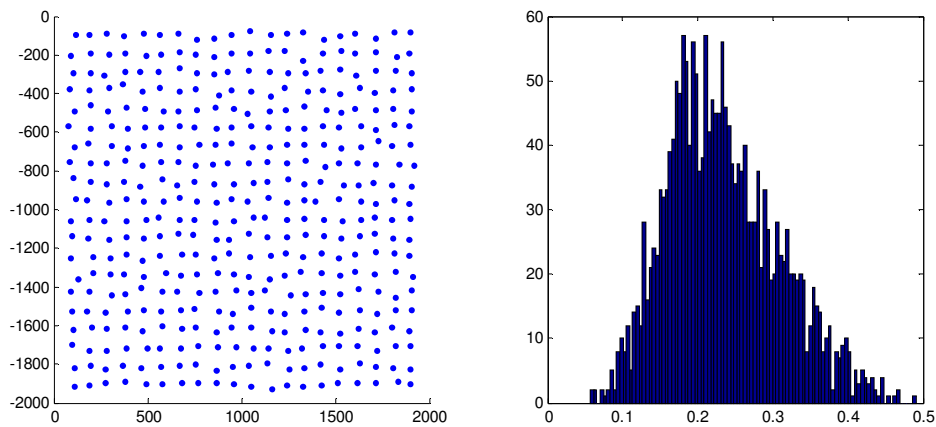


**Figure 7-1.** Hopkins statistics. Simulation of a very well organized lattice of points which even in the existence of Gaussian noise (left) exhibits low H (Hopkins distribution on the right). This shows that Hopkins statistics is not only sensitive at clustering but also at sparseness of points. (Matlab)

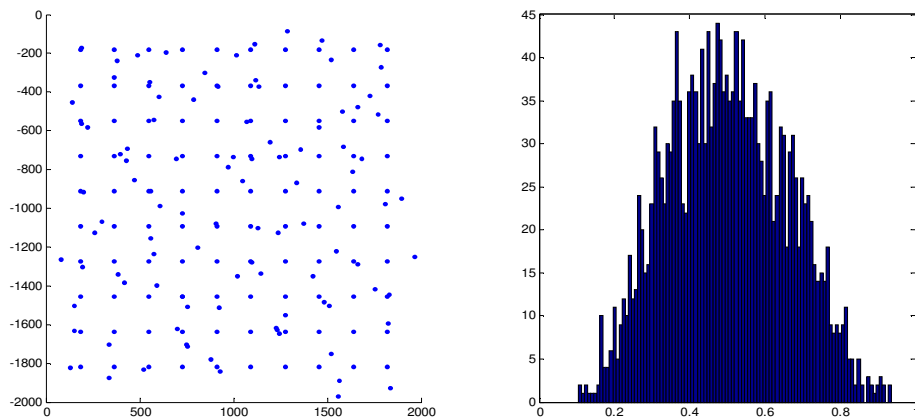


**Figure 7-2.** Hopkins statistics. Simulation of very sparse points with a few clustered (left). Deceptively enough Hopkins distribution (right) has a mean value of 0.50. (Matlab)

## 7.2 Ripley's K function

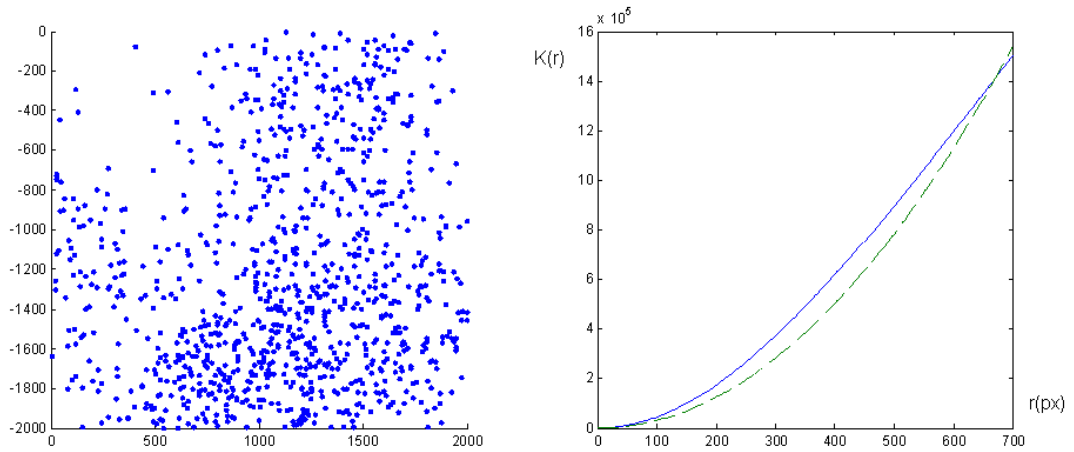


**Figure 7-3.** Ripley's K function. Simulation of randomly centered clusters with Gaussian standard deviation  $\sigma=300$ pixels (left) and the corresponding Ripley's K function (right). The simulated curve exceeds the theoretical curve approximately in the range of  $(\sigma, 2\sigma)$ . (Matlab)

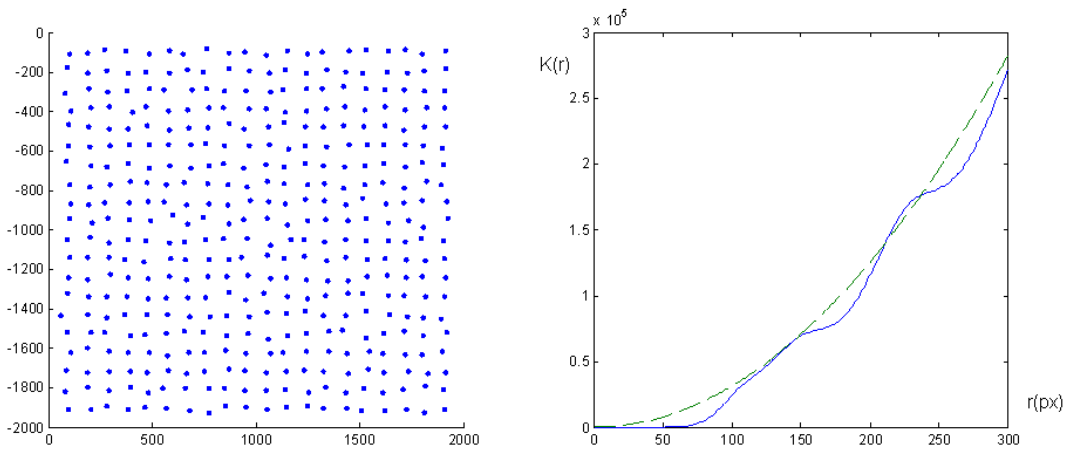


**Figure 7-4.** Ripley's K function. Simulation of sparsely placed particles at distance  $d\sim 100$ pixels (left) and the corresponding Ripley's K function (right). The simulated curve stays below the theoretical curve presenting the first approach of the theoretical curve at approximately  $2d$  and shows an oscillation pattern reflecting the "harmonics" of  $d$ . (Matlab)

### 7.3 Ripley's H function

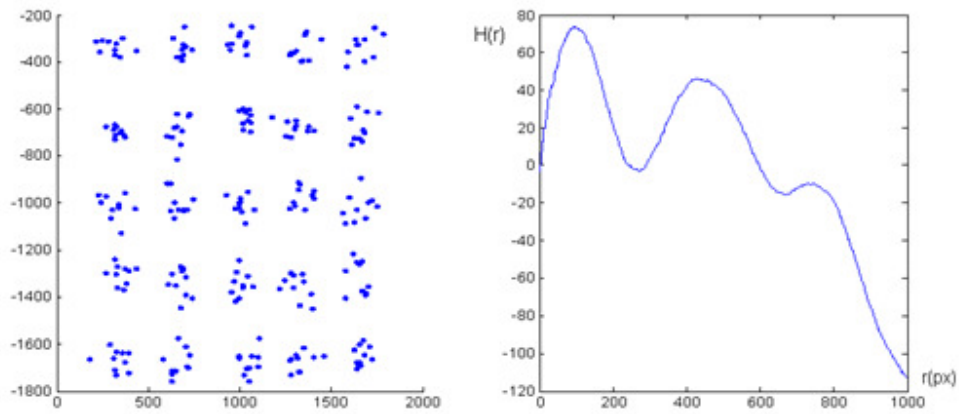


**Figure 7-5.** Ripley's H function. For Gaussian clusters ( $\sigma=50$ ) centered at the vertices of a square lattice with spacing  $a=330$  pixels Ripley's H function presents the first maximum at approximately  $r=2\sigma$ . (Matlab)

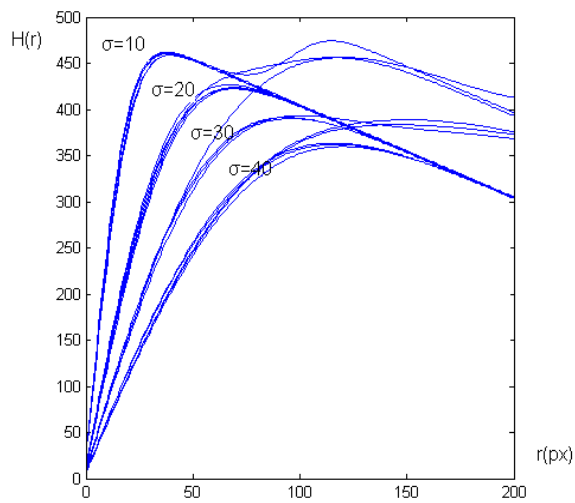


**Figure 7-6.** Ripley's H function. For randomly centered clusters of constant number of particles (although their number did not affect significantly the curves) and Gaussian standard deviation  $\sigma$ , (10, 20, 30, 40) as shown on the diagram, a gradual decrease in the value of maximum is observed with the increase in  $\sigma$ . At the same time the position of the maximum moves to the right with increasing  $\sigma$ . Therefore, an estimation of the cluster size with this diagram seems to be possible. [24] (Matlab)

## 7.4 Simulation Cases Analysis

The Hopkins statistics while being very sensitive to clustering or sparseness does not provide any information on the length scale and it can even out divergence from the CSR case when both clustering and sparseness are present at different scales. This can happen for example in the case of relatively sparse points which are accompanied by closely placed neighbors. The difference of the mean value or the position of the maximum from the value 0.5 could be, in general, an indicator of the percentage of clustered (or sparse) particles in the sample.

It is understood by the analysis of the previously presented simulations that a lot of parameters could affect the shape of Ripley's functions: number of clusters, number of particles in each cluster, dispersion in each cluster, cluster spacing, density etc. The last case (Figure 7-6) presents a relatively simple relation of the cluster size (equivalent to the  $\sigma$  of the Gaussian probability density function) and the position of the maximum. This relation as well as the shape of the graphs is considerably insensitive to cluster spacing (when spacing is large) and local density (10-fold increase in the number of particles in each cluster did not affect the shape of the curves).

Generally, in order to be able to derive useful information from these graphs and quantify the characteristics of the spatial distributions, further analysis of the type conducted in [24] is required. The use of simulated clusters with Gaussian probability seems to be promising as long as a number of variables are thoroughly taken into consideration. Additionally, the employment of inter-particle distance distribution (position of the maximum, for short distances) could provide estimation for the cutoff distance for the clustering analysis. [9][24]

## 8 Discussion

The analysis of the probe densities for both RBL and CHO cell types shows a significant fall after RANTES treatment, something which is in accordance with the theory of induced internalization of the receptors with RANTES. Comparison of the receptor densities between RBL untreated and CHO untreated reveals a significantly reduced number of receptors in the case of CHO cells. Therefore, the expression level of CCR5 in these cells is significantly lower.

The t-test applied for the mean value of the Hopkins statistics in all cases confirms the divergence from the CSR distribution. Therefore, the confirmed sparseness of the RBL untreated group in consideration with the confirmed clustering of the RBL RANTES group implies a significant change between the two spatial distributions.

ANOVA analysis for the mean value of the Hopkins statistics in the CHO cells case between untreated and RANTES does not show what could be characterized as a significant difference in clustering, in the sense that has been discussed in the simulation analysis (i.e. a difference in the percentage of clustered and randomly placed particles). Although the difference of H from the value 0.5 is somehow greater in CHO RANTES, ANOVA does not validate this as significant. The fact that large deviation (with images of very high and images of very low H) is present in both cases may imply that there are larger regions with different spatial characteristics in the same cell group.

The Ripley's K function validates qualitatively the findings of the Hopkins analysis. Ripley's H function furthermore provides some quantitative information derived from the position of the maximum and the height of the maximum which is again in accord with Hopkins analysis.

The sparseness of the receptors may imply the existence of underlying structures on the cell membrane resembling repulsion or relatively dense areas such as lipid rafts. Another aspect that should be taken into consideration is the accuracy of the receptor topography representation through the gold particle topography. The efficiency of the labeling (large particle have lower efficiency) and the fact that one molecule of MC-5 may bind to multiple sites must be considered. The length of antibody may also interfere with the spatial statistics in some cases.

Overall, quantification of the clustering properties in this analysis derived results consistent with the recruitment of receptors in clathrin lattices before the endocytosis.

Further research could include the extension of the analysis to more available data of the same or different conditions; for instance different RANTES stimulation times or use of modified ligands such as AOP RANTES which induce sustained internalization.

## **9 Conclusions**

The study of complex biological mechanisms requires apart from deep biological knowledge, thorough analysis of experimental data, the recruitment of already developed methodologies but also and most importantly interdisciplinary approaches. The use of the specific analytical tools described here, have allowed the extraction of quantified data from micrographs which conventional approaches could not obtain. Furthermore these techniques could be generally applied to address many other biological problems.

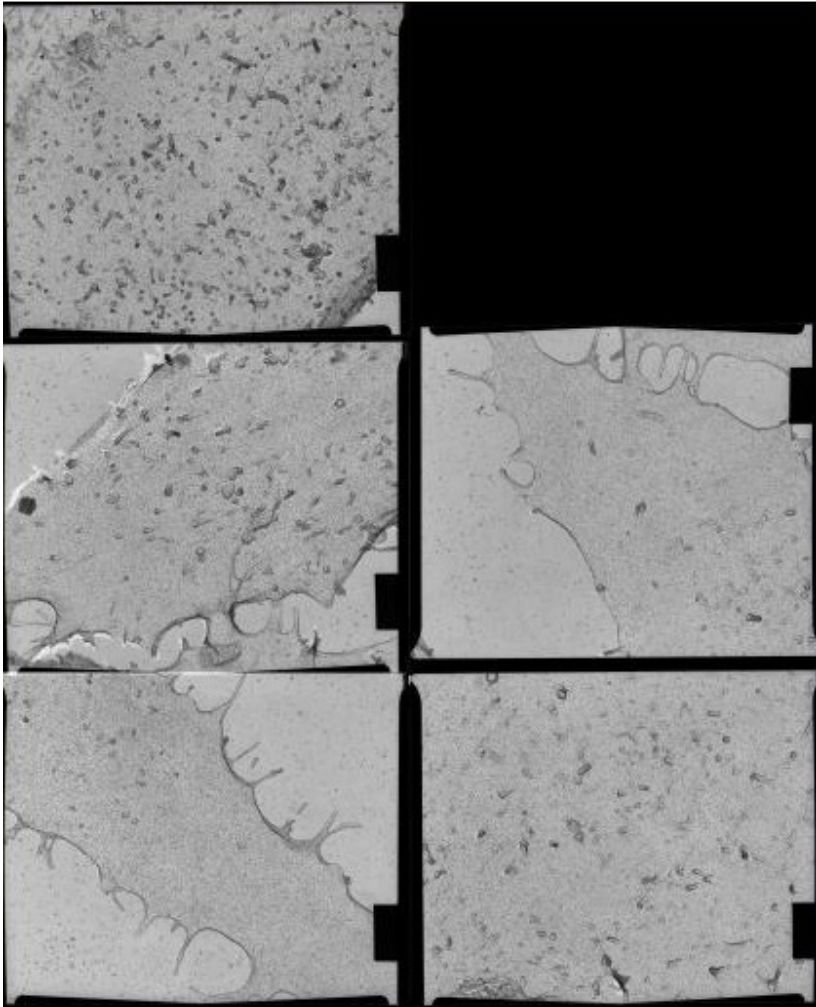
## **10 Acknowledgements**

I would like to thank my two supervisors, Mark Marsh and Lewis Griffin, for their help and guidance during this project and the people at the LMCB, especially Dr Joe Grove, for their help and support. My studying at UCL CoMPLEX is possible because of my scholarship by the Greek State Scholarship Foundation (IKY). CoMPLEX is an EPSRC funded Doctoral Training Centre.

# 11 Appendix (Analyzed Micrographs)

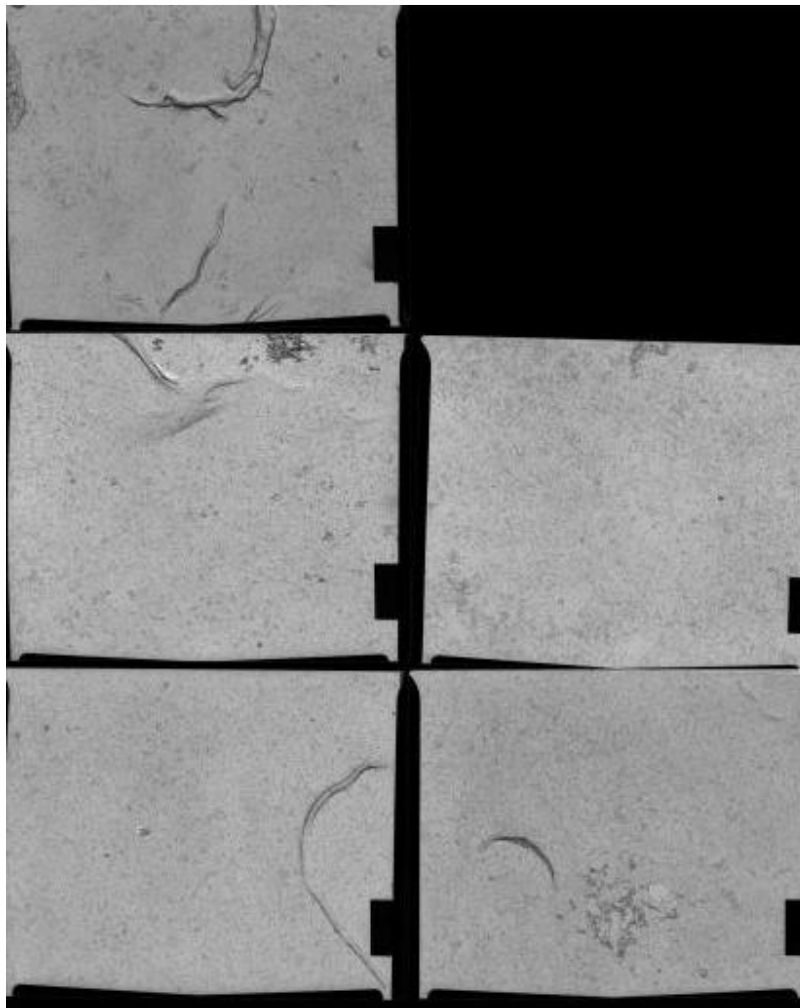
RBL untreated

Micrograph	Data file name
5702, 5703, 5704, 5705, 5708	DATA-07042011-A001



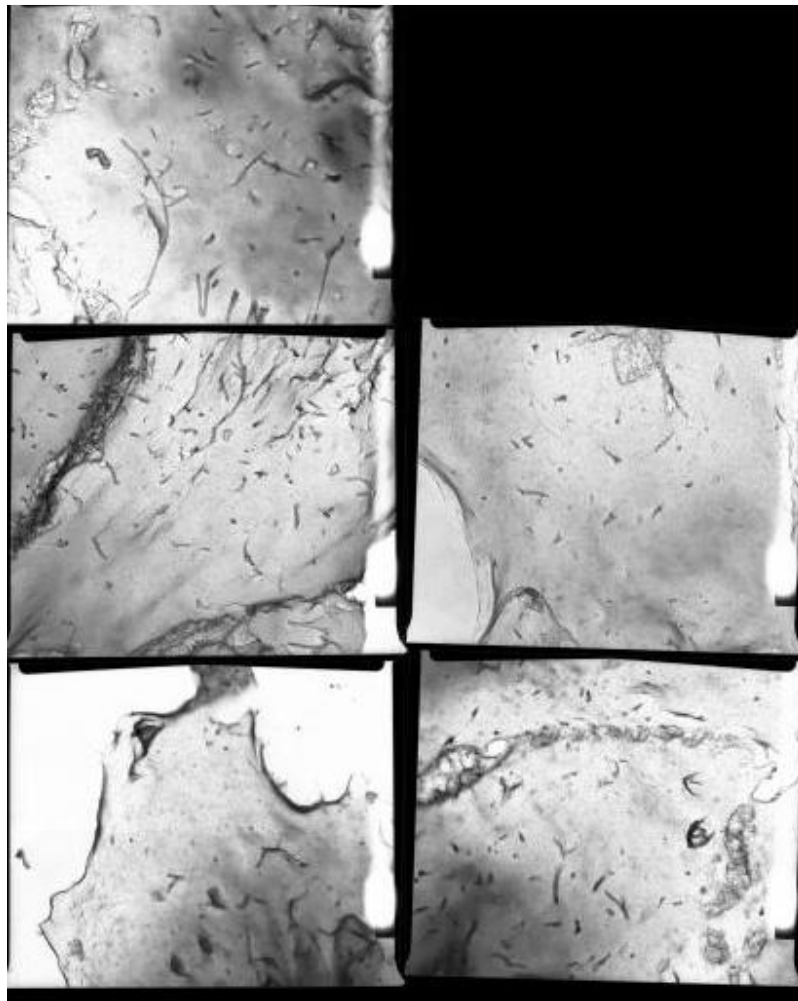
RBL RANTES

Micrograph	Data file name
5727, 5694, 5692, 5691, 5690	DATA-07042011-B001



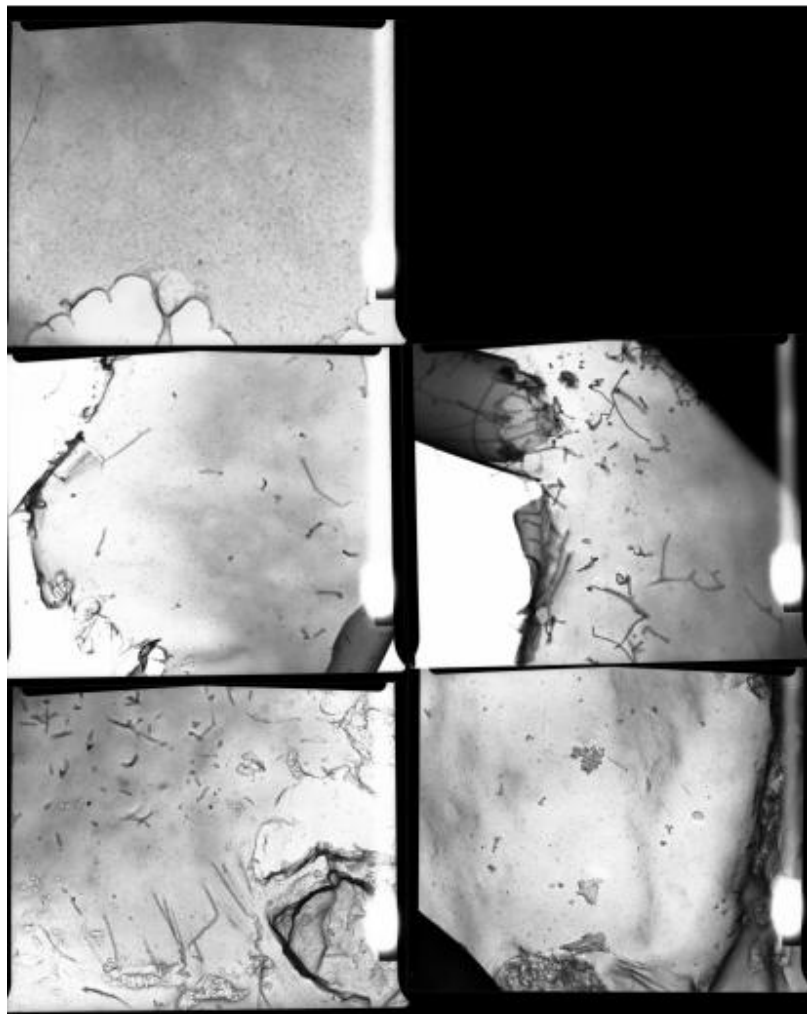
CHO untreated

Micrograph	Data file name
5042, 5043, 5046, 5048, 5049	DATA-07042011-C001



CHO RANTES

Micrograph	Data file name
5026, 5027, 5033, 5031, 5036	DATA-07042011-D001



## 12 References

- [1] S. Wavre, "Endocytic Regulation of Chemokine Receptor Expression," UCL, 2006.
- [2] "AIDS Epidemic Update: December 2009 - Joint United Nations Programme on HIV/AIDS (UNAIDS) and World Health Organization (WHO)." 2009.
- [3] R. W. Doms, "Unwelcome guests with master keys: how HIV enters cells and how it can be stopped," *Topics in HIV Medicine: A Publication of the International AIDS Society, USA*, vol. 12, no. 4, pp. 100-103, Nov. 2004.
- [4] A. Bruce et al., *Essential Cell Biology*, Third. Garland Science, 2010.
- [5] A. Bruce et al., *Molecular Biology of the Cell*, Fifth. Garland Science, 2008.
- [6] J. Grove and M. Marsh, "Virus entry: finding a way in (manuscript in preparation)."
- [7] P. Lajoie, J. G. Goetz, J. W. Dennis, and I. R. Nabi, "Lattices, rafts, and scaffolds: domain regulation of receptor signaling at the plasma membrane," *The Journal of Cell Biology*, vol. 185, no. 3, pp. 381 -385, May. 2009.
- [8] D. Lauffenburger and J. Linderman, *Receptors - Models for Binding, Trafficking and Signaling*. Oxford University Press, 1993.
- [9] J. Zhang, K. Leiderman, J. R. Pfeiffer, B. S. Wilson, J. M. Oliver, and S. L. Steinberg, "Characterizing the topography of membrane receptors and signaling molecules from spatial patterns obtained using nanometer-scale electron-dense probes and electron microscopy," *Micron (Oxford, England: 1993)*, vol. 37, no. 1, pp. 14-34, 2006.
- [10] M. Marsh, *Endocytosis*, First. Oxford University Press, 2001.
- [11] M. Marsh and H. T. McMahon, "The Structural Era of Endocytosis," *Science*, vol. 285, no. 5425, pp. 215 -220, Jul. 1999.
- [12] M. Marsh and A. Helenius, "Virus Entry: Open Sesame," *Cell*, vol. 124, no. 4, pp. 729-740, Feb. 2006.
- [13] J. Levy, H. Fraenkel-Conrat, and R. Owens, *Virology*, Third. New Jersey: Prentice Hall, 1994.
- [14] B. Voyles, *The biology of Viruses*, Second. Mc Graw Hill, 2002.
- [15] E. A. Berger, P. M. Murphy, and J. M. Farber, "CHEMOKINE RECEPTORS AS HIV-1 CORECEPTORS: Roles in Viral Entry, Tropism, and Disease," *Annual Review of Immunology*, vol. 17, no. 1, pp. 657-700, Apr. 1999.
- [16] S. Ugolini, I. Mondor, and Q. J. Sattentau, "HIV-1 attachment: another look," *Trends in Microbiology*, vol. 7, no. 4, pp. 144-149, Apr. 1999.
- [17] K. Miyauchi, Y. Kim, O. Latinovic, V. Morozov, and G. B. Melikyan, "HIV Enters Cells via Endocytosis and Dynamin-Dependent Fusion with Endosomes," *Cell*, vol. 137, no. 3, pp. 433-444, May. 2009.
- [18] J. Daecke, O. T. Fackler, M. T. Dittmar, and H.-G. Kräusslich, "Involvement of clathrin-mediated endocytosis in human immunodeficiency virus type 1 entry," *Journal of Virology*, vol. 79, no. 3, pp. 1581-1594, Feb. 2005.
- [19] J. Mercer, M. Schelhaas, and A. Helenius, "Virus Entry by Endocytosis," *Annual Review of Biochemistry*, vol. 79, no. 1, pp. 803-833, Jun. 2010.
- [20] P. M. Murphy et al., "International Union of Pharmacology. XXII. Nomenclature for Chemokine Receptors," *Pharmacological Reviews*, vol. 52, no. 1, pp. 145 -176, Mar. 2000.

- [21] N. Signoret, L. Hewlett, S. Wavre, A. Pelchen-Matthews, M. Oppermann, and M. Marsh, "Agonist-induced Endocytosis of CC Chemokine Receptor 5 Is Clathrin Dependent," *Molecular Biology of the Cell*, vol. 16, no. 2, pp. 902-917, Feb. 2005.
- [22] N. Signoret et al., "Phorbol Esters and SDF-1 Induce Rapid Endocytosis and Down Modulation of the Chemokine Receptor CXCR4," *The Journal of Cell Biology*, vol. 139, no. 3, pp. 651 -664, Nov. 1997.
- [23] N. Signoret, A. Pelchen-Matthews, M. Mack, A. E. I. Proudfoot, and M. Marsh, "Endocytosis and Recycling of the HIV Coreceptor CCR5," *The Journal of Cell Biology*, vol. 151, no. 6, pp. 1281-1293, Dec. 2000.
- [24] M. A. Kiskowski, J. F. Hancock, and A. K. Kenworthy, "On the use of Ripley's K-function and its derivatives to analyze domain size," *Biophysical Journal*, vol. 97, no. 4, pp. 1095-1103, Aug. 2009.
- [25] B. D. Ripley, "Modelling Spatial Patterns," *Journal of the Royal Statistical Society. Series B (Methodological)*, vol. 39, no. 2, pp. 172-212, Jan. 1977.
- [26] R. Ennos, *Statistical and Data Handling Skills in Biology*, Second. Pearson, Prentice Hall, 2007.